Applied Surface Science 543 (2021) 148698

Contents lists available at ScienceDirect

Applied Surface Science

journal homepage: www.elsevier.com/locate/apsusc

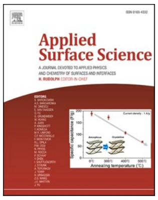

Full Length Article

The layer-by-layer assembly of reduced graphene oxide films and their application as solution-gated field-effect transistors

Fabrício A. dos Santos [a], Nirton C.S. Vieira [b,*], Naiara A. Zambianco [a], Bruno C. Janegitz [c], Valtencir Zucolotto [a]

[a] Nanomedicine and Nanotoxicology Group, Physics Institute of São Carlos, University of São Paulo, CP 369, 13560-970 São Carlos, SP, Brazil
[b] Institute of Science and Technology, Federal University of São Paulo, 12231-280 São José dos Campos, SP, Brazil
[c] Department of Nature Sciences, Mathematics and Education, Federal University of São Carlos, 13600-970 Araras, SP, Brazil

ARTICLE INFO

Keywords:
Reduced graphene oxide
Layer-by-Layer
Transistor
Biosensor
Thin films

ABSTRACT

In this study, graphene oxide (GO) has been reduced in two different ways for the production of oppositely charged reduced graphene oxide (rGO) sheets. One reduction route consisted of the covalent modification of GO with (3-aminopropyl) triethoxysilane and subsequent chemical reduction to produce positively charged rGO. In the second route employed, GO was reduced in a domestic microwave oven, in which the presence of urea doped the material with nitrogen, increasing its electrical conductivity considerably. Multilayers of oppositely charged rGO were manufactured using the layer-by-layer (LbL) assembly technique. The kinetics and growth of multilayers were monitored by UV–Vis absorption spectroscopy and quartz crystal microbalance. rGO multilayers on the interdigitated gold electrodes originate high conductive films, in which the number of deposited layers controls the conductivity. As a solution-gated field-effect transistor, the devices presented high transconductance; (90 μS and 55 μS for holes and electrons, respectively). Upon modification of the LbL films with papain, used as a biological recognition element, the devices were capable of detecting Cystatin C protein (a chronic renal disease biomarker) in synthetic urine in concentrations as low as 5 $ng.mL^{-1}$. Therefore, the proposed transistors proposed here represent interesting alternatives as novel sensors and biosensors platforms.

1. Introduction

The pioneering study of graphene by Novoselov and co-workers opened the way for the development of new organic optoelectronic devices, increasing the advances in both Materials Science and Condensed Matter Physics areas [1]. Mechanical exfoliation of graphite and chemical vapor deposition (CVD) are the well-established techniques for graphene production. Each one has unique characteristics in terms of cost, quality, and processability. Mechanical exfoliation, for example, produces graphene of the highest quality [1] but is not suitable for mass production since it has low yield and reproducibility. CVD is an adequate technique for large scale production of graphene with a surface coverage of almost 100% over large areas [2]. However, this is very costly and produces graphene with lower quality as compared to the mechanical exfoliation.

Chemical exfoliation of graphite to graphene oxide (GO) has been proving to be an alternative for mass production of graphene derivatives at a low cost [3]. GO exhibits oxygen-containing functional groups in its basal plane and borders having a mixture of carbon atoms with sp^2 and sp^3 hybridization, resulting in insulating characteristics [3]. The partial reduction of functional groups produces another graphene derivative, namely, reduced graphene oxide (rGO), which presents π conjugated structure and consequent electrical conductivity [4]. Furthermore, the functional groups remaining during the reduction process facilitates its dispersion in various solvents, including water. The latter fact allows the deposition of rGO on different substrates and surfaces. In other words, although the conductivity of rGO is lower than that of pristine graphene, this material is a good alternative for applications in optoelectronic devices, especially in terms of cost and processability, as in the case of its use in transistors [5], photodetectors [6] and sensors/biosensors [7].

Sensors and biosensors, in particular, stand out the devices using graphene or rGO as active materials in solution-gated field-effect transistors (FETs) [8]. These devices present high sensitivity for various analytes and operate at low gate potentials due to the nanosized electrical double layer (EDL) at the graphene/solution interface [8]. There is a broad range of applications of rGO as FET-based sensors including: (i)

---

* Corresponding author at: Institute of Science and Technology, Federal University of São Paulo, 12231-280 São José dos Campos, SP, Brazil (Nirton C. S. Vieira).
E-mail address: ncsvieira@unifesp.br (N.C.S. Vieira).

https://doi.org/10.1016/j.apsusc.2020.148698
Received 17 August 2020; Received in revised form 2 December 2020; Accepted 3 December 2020

the detection of new analytes such as biomarkers for diagnosis [9], (ii) the use of new receptors for (bio) molecular recognition, aiming to increase selectivity [10], and (iii) innovations in the method of manufacturing the transistors [11].

Electrostatic layer-by-layer (LbL) self-assembly is a powerful technique that combines effectiveness and low cost in the manufacture of thin films, with rigorous control of the deposition of layers at the molecular level [12]. Due to the versatility of this technique, various organic and inorganic materials can be combined with GO or rGO, resulting in self-assembled composites with distinct and unique properties for the most diverse applications [12]. Transparent and conductive films to be used in organic light-emitting diode, for example, have been fabricated by Lee et al. through the alternating adsorption of positively/negatively charged rGO sheets [13]. In another study, Hwang et al. demonstrated the manufacture of solid-state transistors using the same methodology [14].

In this paper, we report on the reduction of GO to produce oppositely-charged rGO sheets and their subsequent self-assembly on interdigitated electrodes for solution-gated FETs fabrication. The device layout can be seen in Fig. S1. The number of rGO layers controls the conductivity of devices. The feasibility of the solution-gated FETs as sensors was demonstrated. As a proof-of-concept, we have shown that the devices can discriminate between solutions with different saline concentrations, and, when modified with papain, can detect levels of a renal disease biomarker (Cystatin C protein) in synthetic urine.

2. Experimental

2.1. Chemicals

Expanded graphite (purity > 99.5%) was kindly provided by Nacional de Graphite Company (Brazil). All chemicals, including papain and PBS (phosphate-buffered saline), were purchased from Sigma-Aldrich (USA) and used as received without further purification. Human Cystatin C protein was supplied by Fitzgerald (USA). Artificial human urine was prepared according to the literature at pH 6.4 [15].

2.2. Preparation of negatively and positively charged rGO

GO was produced by the modified Hummers method using expanded graphite as the precursor. Details on the GO synthesis and its characterization can be found elsewhere [16]. We used an adapted methodology of Umrao and coworkers by using urea as a nitrogen source for the production of negatively charged rGO (rGO-N) [17]. Briefly, 10 mg of urea was added to 100 mL of GO aqueous dispersions (1.0 mg.mL^{-1}) and homogenized in an ultrasonic bath for 2.5 h. After drying, the obtained powder was irradiated using a microwave oven during 10-second intervals, followed by cooling. Total irradiation time was one minute at a power of 700 W. The product was dispersed in ultrapure water by ultrasonication for 2 h and dialyzed for 24 h to remove the remaining urea and byproducts.

Positively charged rGO (rGO-SiNH$_2$) was obtained by covalently bound of (3-aminopropyl) triethoxysilane (APTES) to GO sheets adapting the methodology of Kim et. at. [18], followed by chemical reduction with sodium borohydride (NaBH$_4$). First, 10 mg GO was dispersed in 100 mL dimethylformamide in an ultrasonic bath. 3 mL of APTES was added to the GO dispersion under stirring, followed by heating at 70 °C for 2 h. The temperature was increased to 95 °C, and 3 g of NaBH$_4$ was added in the dispersion, remaining under stirring for 2 h. The dispersion was cooled at room temperature and centrifuged for 10 min at 10,000 rpm, changing the solvent to acetone. Finally, the obtained rGO-SiNH$_2$ dispersion was dialyzed for 24 h in ultrapure water to remove any residues of organic solvents and byproducts.

The synthesized materials were characterized by ultraviolet–visible absorption spectroscopy (U-2900 Hitachi, Japan), Fourier-transform infrared spectroscopy (Nicolet iS50, Thermo Scientific, USA), zeta potential measurements (Zetasizer ZS90, Malvern Instruments, UK), and X-ray photoelectron spectroscopy (K-alpha XPS Thermo Scientific, USA). For XPS analyzes, the samples were prepared on a Si/SiO$_2$ substrates by drop-casting. 50 μL of the dispersion (0.2 mg.mL^{-1}) of each material (rGO-SiNH$_2$ or rGO-N) were deposited on the substrates and dried at room temperature under vacuum. Three measurements were performed in different regions of each sample.

Atomic Force Microscopy (AFM) was also used to characterize the films on B270 glass substrates. AFM images were taken in FlexAFM equipment (Nanosurf) using general-purpose cantilever TAP-300 (budget sensors) in tapping mode. The images and statistics were treated using Gwyddion software.

2.3. Interdigitated gold electrodes

Interdigitated gold electrodes were fabricated by conventional photolithography using the facilities of the Microfabrication Laboratory (LMF) of the Brazilian Nanotechnology National Laboratory (LNNano). The electrodes contain 30 pairs of gold fingers (5 mm length) with width and spacing of 50 μm between them. The thickness of the fingers is composed of 20 nm of chromium (used as an adherent layer) covered with 130 nm of gold; both deposited via DC sputtering on B270 glass slides.

2.4. Fabrication and functionalization of the LbL films

Before LbL assembly, the substrates (quartz slides and interdigitated electrodes) were previously hydrophilized with a 2% KOH alcoholic solution for 5 min, followed by exhaustive washing in ethanol and ultrapure water. The substrates were first immersed in the dispersion of rGO-SiNH$_2$ (0.2 mg.mL^{-1}, pH 3.0) for 60 min. The substrates were then washed in water for 1 min and gently dried with N$_2$ flow. The next layer was deposited upon immersing the substrate in rGO-N (0.2 mg.mL^{-1}, pH 3.0) for 15 min, followed by washing in water for 1 min and drying with N$_2$ flow. The process was repeated to the desired number of bilayers. At the end of the LbL assembly, the films were dried at 150 °C for 3 h.

For Cystatin C detection experiments, papain was immobilized on 4.5-bilayer (rGO-SiNH$_2$/rGO-N) films (*i.e.*, films containing 4 complete rGO-SiNH$_2$/rGO-N bilayers plus a rGO-SiNH$_2$ layer) using glutaraldehyde as the crosslinker [19–21].

2.5. Electrical characterization

$I \times V$ curves were taken using a source measure unit (Keithley 2612A) controlled via a personal computer. Electrical measurements were performed at room temperature to determine the resistivity of the self-assembled films on the interdigitated electrodes. In this case, drain-source voltage (V_{DS}), *i.e.*, the voltage between the interdigitated gold fingers containing (rGO-SiNH$_2$/rGO-N) was varied. As a solution-gated FET configuration, a PBS solution (pH 7.4) was used, and the devices are gated via a silver/silver chloride (Ag/AgCl) reference electrode. Transfer curves were obtained by varying gate-source voltage (V_{GS}) while keeping V_{DS} constant. V_{GS} represents the voltage between the reference electrode and one of the contacts from the interdigitated electrode.

For testing as ionic sensors, the devices were also electrically characterized in PBS with different ionic strengths. For the detection of Cystatin C, transfer curves were taken in diluted synthetic urine containing different concentrations of Cystatin C.

3. Results and discussion

3.1. Characterization of negatively and positively charged rGO

Fig. 1a shows the UV–Vis absorption spectra of rGO-SiNH$_2$ and rGO-N dispersions in ultrapure water. The GO absorption spectrum is also

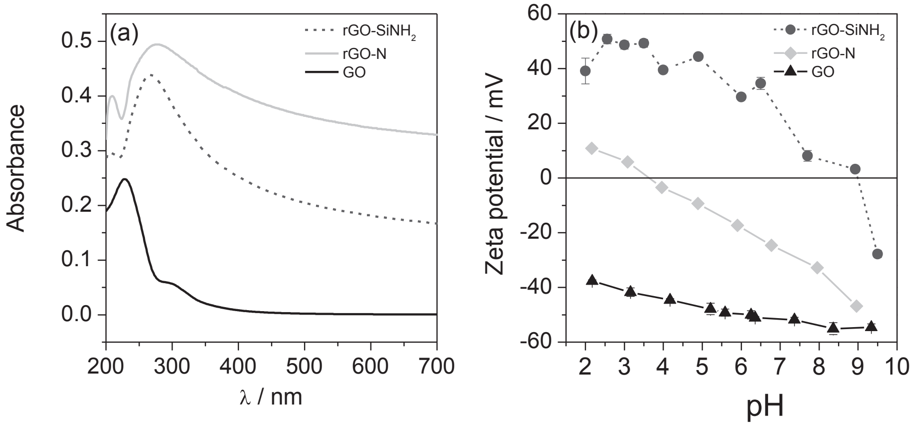

Fig. 1. (a) Absorption spectra of rGO-SiNH$_2$, rGO-N, and GO dispersions in ultrapure water and (b) Zeta potential of GO, rRGO-SiNH$_2$ and rGO-N dispersions under different pH conditions (b).

shown for comparison. Absorption bands at ca. 268 nm and 275 nm are observed in rGO-SiNH$_2$ and rGO-N, respectively. The absorption spectra indicate that the reduction of the GO occurred in both cases since there was the disappearance of the shoulder around 300 nm, characteristic of transitions n → π* of the C═O bonds in the GO. After the reduction, the hexagonal network is partially reconstituted, since it had a redshift of the typical GO band in 230 (corresponding to the π → π* transitions of the C═C bonds of the aromatic ring) [16]. For microwave-performed reductions, doping takes place through chemical element exchange. Sites occupied by oxygen are replaced by nitrogen due to the high temperatures involved in the reduction process [17].

Zeta potential measurements were used to investigate the surface charge of GO, rGO-N, and rGO-SiNH$_2$ suspensions at different pH values. Fig. 1b shows how the zeta potential varies as a function of pH (from 2.0 to 9.5) for rGO-SiNH$_2$, rGO-N, and GO dispersions. As prepared, GO is negatively charged in a broad pH scale due to the presence of oxygen-containing functional, mainly hydroxyl and carboxylic acid groups [12]. The maximum stability of the rGO-SiNH$_2$ is obtained at pH from 2.5 to 3.5, and the isoelectric point is at ca. pH 9.0. We can consider that the APTES bound to the GO, leaving exposed -NH$_3^+$ groups, which confer the positive surface potential [22]. Although the net surface charge is positive relative to the acidic pH range, the coverage of rGO with APTES was not complete due to the presence of unbound phenolic groups, which explains the rGO-SiNH$_2$ stability in basic pH values [23]. For rGO-N, Fig. 1b indicated less stability compared to the GO. This is due to the decrease of the oxygenated functional groups during the reduction. However, rGO-N showed good stability at basic pH range, due to the presence of remaining hydroxyl groups, exhibiting an isoelectric point at ca. pH 3.5. As we shown in the next section (Fig. 4 a and b), that the ideal pH for the LbL assembly of (rGO-SiNH$_2$/rGO-N) was 3.0. At this pH value, the zeta potential is slightly positive for rGO-N, and even under this condition, an efficient film deposition was observed.

XPS measurements were taken to confirm the GO reduction and nitrogen doping in rGO-N, as well as to confirm the functionalization of rGO-SiNH$_2$ with APTES. Fig. 2a, b and c show the general survey XPS spectra for GO, rGO-N, and rGO-SiNH$_2$, respectively. As expected, nitrogen doping has been successful in rGO-N. Besides, the presence of silicon in rGO-SiNH$_2$ confirms the functionalization with APTES.

There was a significant decrease in the amount of oxygen in the two samples compared to GO (see Table S1). This decrease was smaller in rGO-SiNH$_2$, due to the covalent bond between Si and O atoms. In the rGO-N, there was a decrease in the amount of oxygen and an increase in the incorporation of nitrogen. These values are compatible with other methods of GO reduction/doping using urea [24], and superior to other processes where ammonia was used as a source of nitrogen [17,25,26].

Fig. 2d, e and f show the high-resolution XPS spectra of C 1s for GO, rGO-N, and rGO-SiNH$_2$, respectively. For GO (Fig. 2d) the three peaks are related to the bindings C—C/C═C (284.3 eV), C—O (286.3 eV) and C═O (287.5 eV) [27]. The relative intensities of the last two peaks decrease after the reduction for rGO-N, as shown in Fig. 2e, where the four peaks are corresponding to the bindings C—C/C═C (284.1 eV), N—sp^2 (285.5 eV), N—sp^3 (286.5 eV) and —C═O (288.8 eV) bonds [17,28]. Four peaks are observed in Fig. 1f related to the bindings C—C/C═C (284.3 eV), C—O (286.3 eV), C═O (288.2 eV), π → π* shake-up satellite, indicating the formation of an aromatic or conjugated system (292.5 eV) [29,30]. For comparison, the percentage of each C 1s bond is shown in Table S2. Note that the restoration of the crystalline network had a significant increase in the two reduction processes, and this increase was more considerable for the rGO-N. Fig. 2g shows the high-resolution XPS spectra of N 1s deconvoluted into three peaks; pyridinic N (398.1 eV), pyrrolic N (400 eV) and graphitic N (402 eV) [17], and the proportion of the bonds are 22.6%, 74.9%, 2.5%, respectively. The peaks for rGO-SiNH$_2$ are shown in Fig. 2h, which correspond to C-NH$_2$ (399.3 eV) and protonated amine C-NH^{3+} (401.3 eV), in the proportions of 42.4% and 57.6% respectively [31].

The synthesized materials were also characterized by Fourier-transform infrared spectroscopy (FTIR), as present and discussed in the Supplementary Information, Fig. S2.

3.2. Characterization and optimization of LbL assembly

The adsorption time and the pH for both rGO-SiNH$_2$ and rGO-N dispersions were investigated to optimize the LbL assembly. Quartz crystal microbalance was used to monitor the amount of adsorbed material on the electrode surface at each deposition step. As shown in Fig. 3a, the time required to reach maximum material adsorption was 60 min for the rGO-SiNH$_2$ positive layer. Following deposition and washing, rGO-N was added to form the negative layer onto rGO-SiNH$_2$, with time to reach maximum adsorption of ca. 15 min (Fig. 3b). Sixty and 15 min were then considered as optimal times for the adsorption in the LbL assembly of (rGO-SiNH$_2$/rGO-N) bilayers on quartz slides and interdigitated electrodes.

Fig. 4 shows how the intensity of the absorption bands for rGO-SiNH$_2$ (Fig. 4a) and rGO-N (Fig. 4b) varied at different pH values. UV–Vis spectra were taken after immersion of the quartz substrate initially into the rGO-SiNH$_2$ dispersion (0.2 mg.mL^{-1}) for 60 min, followed by immersion of the same substrate (pre-coated with a rGO-SiNH$_2$ layer) into the rGO-N dispersion (0.2 mg-mL^{-1}) for 15 min, after the washing and drying steps. In pH 3.0, the potential of the rGO-N is slightly positive (see Fig. 1b), and even under this pH condition, a higher rGO-N adsorption was verified on the quartz/rGO-SiNH$_2$ film, which is probably because adsorption is driven by H-bond, rather than electrostatic

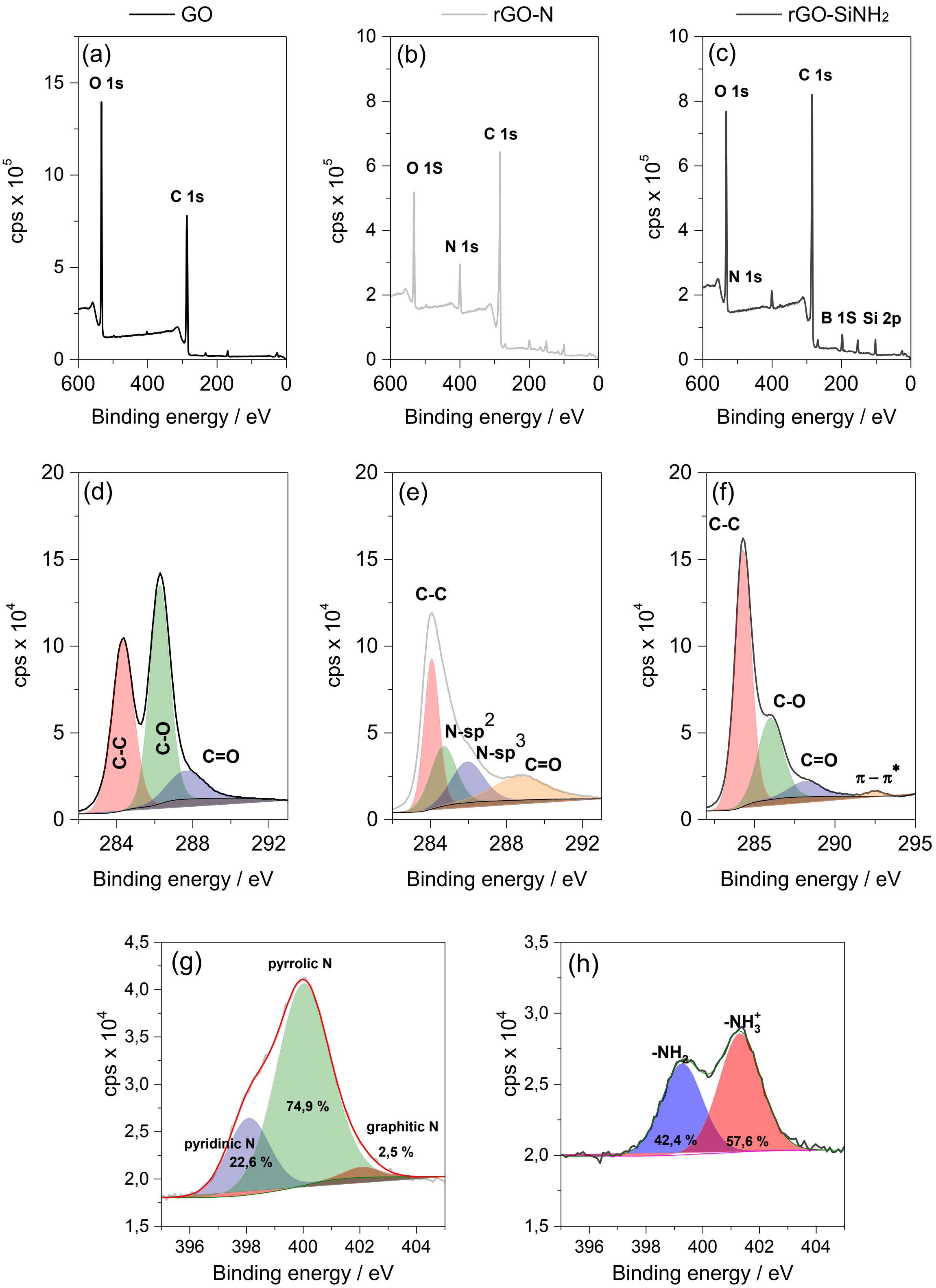

Fig. 2. General survey XPS spectra for (a) GO, (b) rGO-N, and (c) rGO-SiNH$_2$. High-resolution XPS spectra of C 1s for (d) GO, rGO-N, and (f) rGO-SiNH$_2$. High-resolution XPS spectra of N 1s for (g) rGO-N, and (h) rGO-SiNH$_2$.

interactions.

UV–Vis spectroscopy was also used to monitor the growth of LbL films on quartz substrates under the optimized conditions. Fig. 4c shows the UV–Vis spectra as a function of the number of (rGO-SiNH$_2$/rGO-N) bilayers. Fig. 4d shows that the absorption band at 268 nm varied linearly with the number of bilayers up to five bilayers, indicating that the same amount of (rGO-SiNH$_2$/rGO-N) was adsorbed at each assembly step, which is in accordance to the literature [12].

Fig. S3 shows AFM images for films containing one, three, and five (rGO-SiNH2/rGO-N) bilayers. The images show the films surface

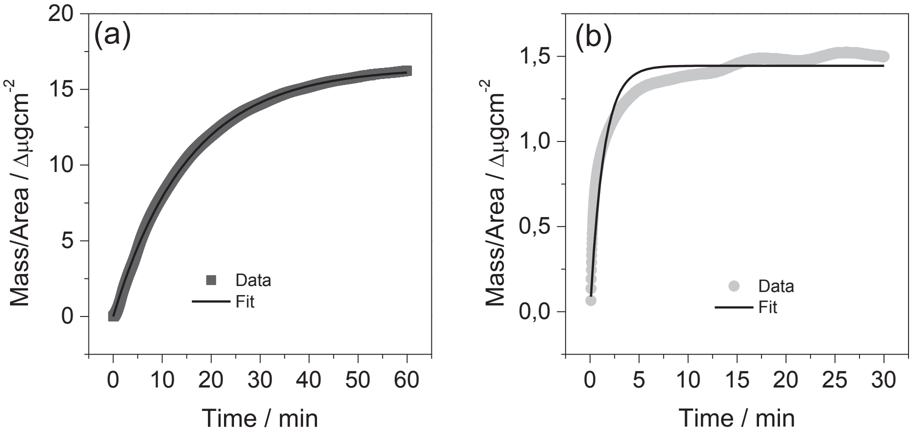

Fig. 3. Adsorption curves using quartz microbalance for the (a) rGO-SiNH$_2$ and (b) rGO-N.

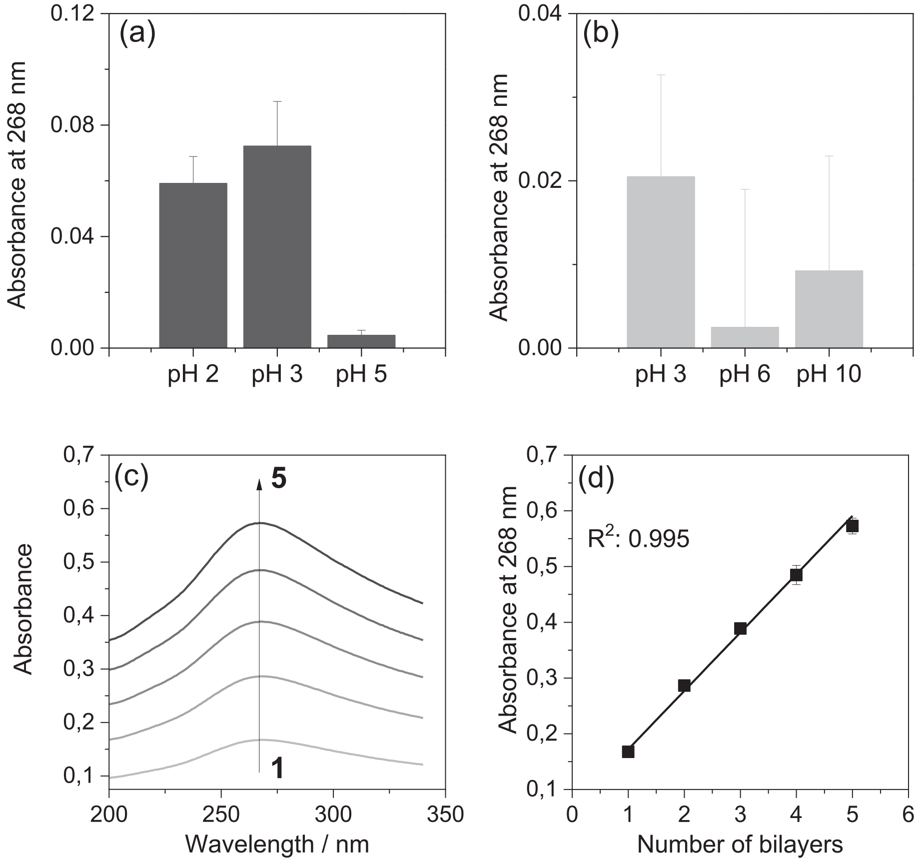

Fig. 4. UV–Vis study of the pH influence on the adsorption of (rGO-SiNH$_2$/rGO-N) LbL films. The growth was monitored by absorbance at 268 nm for the (a) rGO-SiNH$_2$ and (b) rGO-N. Absorbance shown in (b) was subtracted from absorbance value in (a). (c) UV–Vis spectra of (rGO-SiNH$_2$/rGO-N) LbL films. (d) The linear dependence of the absorption at 268 nm with the number of bilayers (rGO-SiNH^2/rGO-N). Error bars represent the standard deviation of three different films.

containing some aggregates. Upon increasing the number of bilayers, the aggregates size also increased. We cannot estimate the thickness of the bilayers due to the surface irregularities from the substrate used (B270 glass).

3.3. *Electrical characterization of (rGO-N-SiNH$_2$) LbL films*

The (rGO-SiNH$_2$/rGO-N) LbL films were grown on gold interdigitated electrodes for electrical characterizations. Fig. 5a shows the representative $I \times V$ curves for films containing one, three and five (rGO-SiNH$_2$/rGO-N) bilayers. Then $I \times V$ curves exhibit a linear behavior, which is indicative of a good contact between the (rGO-SiNH$_2$/rGO-N) films and the metallic fingers, even for one bilayer. The calculated electrical resistances were 10, 1.5 and 1.0 kΩ for one, three and five-bilayer films, respectively, suggesting that the resistance decreases as the bilayers increase. We did not investigate films containing more than five bilayers.

The same synthesis/modification of negatively and positively charged rGO was applied to the manufacture of LbL films. In the other words, the experimental conditions for reducing GO were maintained and the formation of LbL films was explored. A variation in the reduction state of the films would result in a change in their electrical properties.

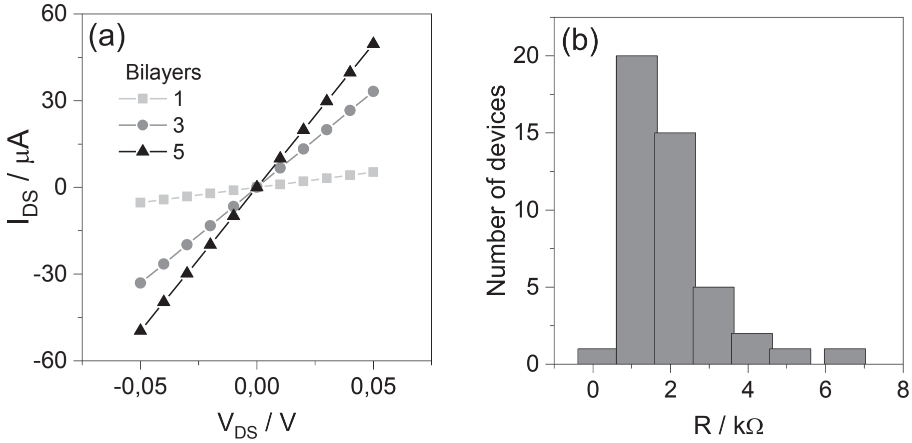

Fig. 5. (a) Representative $I \times V$ curves for films containing one, three and five (rGO-SiNH$_2$/rGO-N)) bilayers. (b) Distribution of the resistance values from a sample of 45 devices containing five bilayers.

As a result, the $I \times V$ curves of different five-bilayer films, manufactured in different days are shown in Fig. S4. The error bars represent the average values of four different films measured each day. It is noted that there was no significant variability between the different devices within the conditions proposed here.

After the LbL assembling on interdigitated electrodes, the films exhibited a high electrical resistance (ca. 26 MΩ, see Fig. S5). After drying the films at 150 °C, a significant decrease in the resistance values was observed. As water is involved in the LbL assembly, it is not surprising that adsorbed water can play an important role. The reduction in the resistance values observed in all situations is mainly due to the evaporation of the water, which act as load scattering centers, thus decreasing the electrical conductivity of non-dried films. When dried, the particles are packed, making the films more compact, reducing the roughness, and increasing the packing of the sheets of rGO-SiNH$_2$ and rGO-N and consequently the contact between them. Fig. 5b shows that

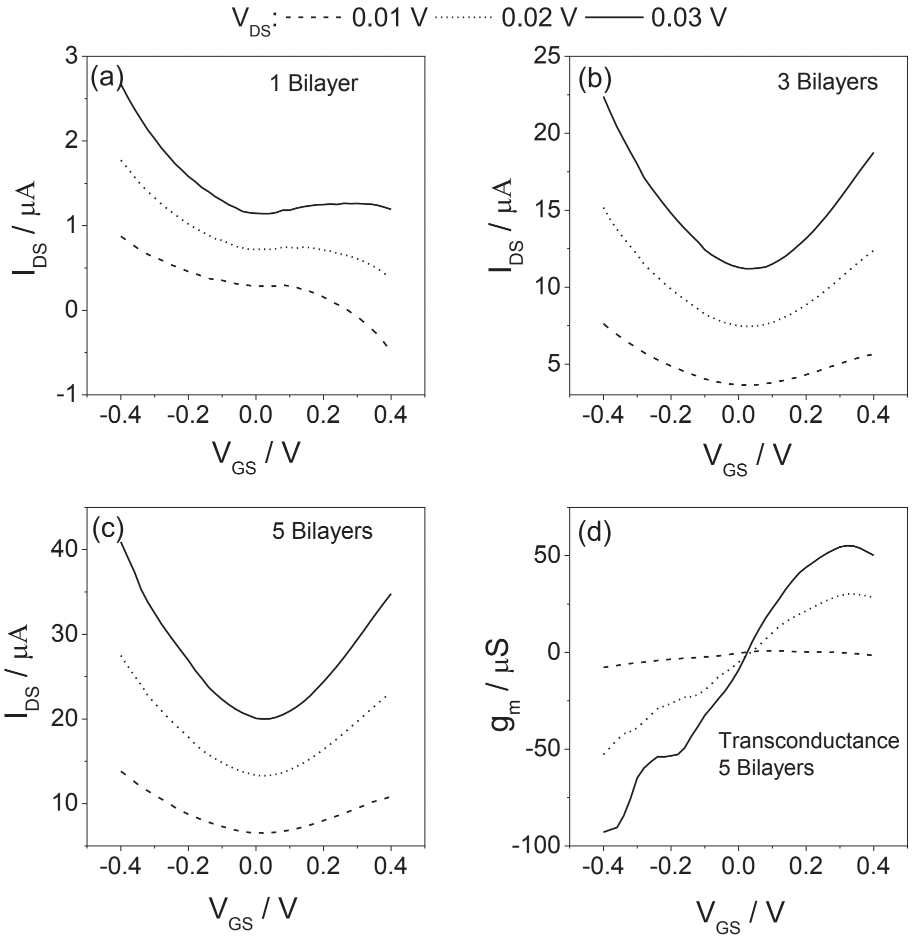

Fig. 6. Transfer curves for (rGO-SiNH$_2$/rGO-N) LbL transistors containing (a) 1, (b) 3 and (c) 5 bilayers for different V_{DS} values (10, 20 and 30 mV). (d) Transconductance of 5-bilayer (rGO-SiNH$_2$/rGO-N) at V_{DS} = 30 mV.

the resistance average is 1.5 kΩ from a set of 45 five-bilayer films.

The electrical resistance was monitored during the LbL assembly to prove the hypothesis previously mentioned. In this context, after the deposition of each material layer (rGO-SiNH$_2$ or rGO-N), the resistance values were measured without drying. Fig. S5 shows that the resistance decreases as a function of the number of layers. After the seventh layer, it is observed that there was no significant variation in resistance values for the films without drying, corroborating that this effect was due to the materials organization on the interdigitated electrodes as the number of layers increases.

The (rGO-SiNH$_2$/rGO-N) LbL films were also applied as a solution-gated FETs. In this case, the gate voltage is applied via the Ag/AgCl reference electrode positioned on the top of the electrolytic solution (PBS) deposited directly on the interdigitated electrodes containing the (rGO-SiNH2/rGO-N) LbL films. The contacts of the interdigitated electrode act as the source and drain of the transistor. The EDL that was formed on the LbL film/solution behaves as a gate insulator, similar to a solid-state gate dielectric in a conventional transistor [2].

Transfer curves measured in PBS for LbL transistors containing 1, 3 and 5 rGO-SiNH$_2$/rGO-N bilayers are displayed in Fig. 6. One-bilayer films showed a unipolar conduction, *i.e.* the conduction is predominantly by holes (Fig. 6a). Hwang et. al. observed a similar effect for one-bilayer solid-state rGO transistors, and the explanation for this phenomenon was the positive charge transfer from the substrate to the LbL film during heat treatment at 1000 °C [13]. In our case, the positive material (rGO-SiNH$_2$) is more prevalent in LbL film, as shown earlier by quartz microbalance adsorption kinetics (Fig. 3), which explains the unipolar character for the one-bilayer films. As shown in Fig. 5b and c, for 3 and 5 rGO-SiNH$_2$/rGO-N bilayers films, respectively, transfer curves displayed a graphene-like transistor behaviour, where the conductivity is modulated by the gate voltage around a point of minimum conductivity [1,2].

The FET transconductance, defined as ($gm = dI_{out}/dV_{in}$), represents their amplification capability. In this study, transconductance was calculated from the numerical derivative of the transfer curves for films containing 1, 3 and 5 rGO-SiNH$_2$/rGO-N bilayers. Fig. 6d shows that transconductance was dependent on the number of (rGO-SiNH$_2$/rGO-N) bilayers. Transconductance values up to 90 μS and 55 μS (for holes and electrons, respectively) could be achieved for 5-bilayer films. Solution-gated rGO FETs with high transconductance values (up 800 μS) can be found in the literature [32]. However, these higher *gm* values were obtained at $V_{DS} = 0.1$ V, ca. 3 times higher than the range used in the present study.

3.4. (rGO-N-SiNH$_2$) LbL transistors as sensor and biosensor

To demonstrate their potential application as sensors, transfer curves were taken for the (rGO-SiNH$_2$/rGO-N) LbL FETs, immersed initially in PBS with different ionic strengths. The results are displayed in Fig. 7a. As it is known, the PBS ionic strength affects the EDL, causing the differences in the transfer curves [2]. According to Debye-Hückel theory, the EDL has values of ca. 0.7, 2.3, and 7.3 nm for 150, 15, and 1.5 mM PBS solution [33]. The variation in Debye length changes the capacitance and, consequently, how V_{GS} drops across at the solution/gate and solution/(rGO-SiNH$_2$/rGO-N) interfaces [2].

It is known that when cystatin C binds the catalytic center of papain, it inhibits its enzymatic action [34]. Papain has been used as an element of biological recognition in electrochemical biosensors and other detection assays of cystatin C [35,36]. Here, 4-bilayer rGO-SiNH$_2$/rGO-N films - containing an additional layer of rGO-SiNH$_2$ - were functionalized with papain, and detection of cystatin C was evaluated in 100-folder diluted synthetic urine. Dilution was necessary to overcome the detection limitations imposed by Debye length in FET-based affinity biosensors [20]. Fig. 7b shows the transfer curves, in which V_{GS} voltage varied from −0.2 to 0.2 V. Since Papain isoelectric point is between pH 8.75–9.55 [37], in the pH 6.4 (pH of the synthetic urine), the papain-cystatin C complex is positively charged. The I_{DS} current decreases upon increasing the amount of cystatin C, and the voltage at the minimum conductivity point shifts to positive values, as shown by Kim and coworkers for the detection of antibody-antigen interactions using rGO FETs [38]. These results confirmed that the devices proposed here are functional and may find applicability as biosensors.

4. Conclusions

Oppositely charged reduced graphene oxides were self-assembled on different substrates by the LbL technique, characterized and applied as solution-gated field-effect transistors. Zeta potential measurements indicated that pH 3.0 is the best condition for the LbL films assembly. The electrical properties of (rGO-SiNH$_2$/rGO-N) LbL films were dependent on the number of deposited layers. Drying the films at 150 °C considerably increased the conductivity of self-assembled films deposited on interdigitated electrodes. (rGO-SiNH$_2$/rGO-N) LbL FETs presented high transconductance values. We have also shown the devices can be applied as a biosensor for Cystatin C detection in synthetic urine, which is important since Cystatin C may act as an indicator of chronic renal disease. The simplicity of the devices combined with the low cost of producing chemically exfoliated graphene oxide can, therefore, be explored for the production of electronic devices with specific functionalities. This opens the way for the development the low-cost sensors

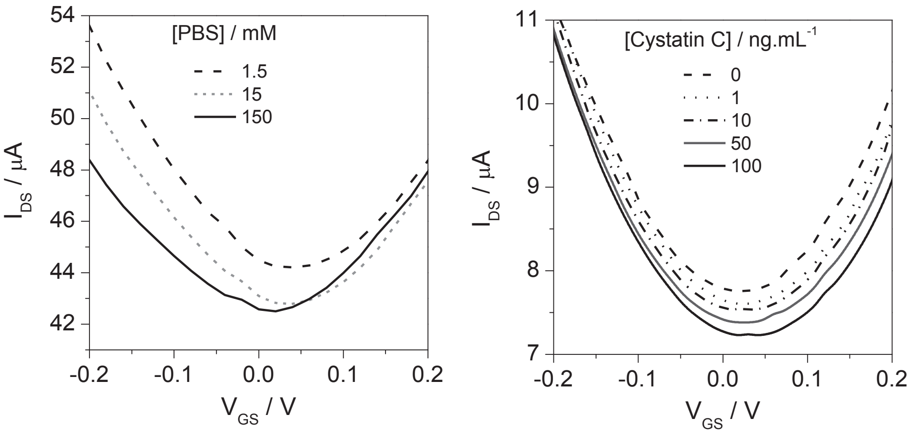

Fig. 7. (a) Transfer curves of (rGO-SiNH$_2$/rGO-N) LbL FETs in different ionic strengths of PBS (1.5, 15, and 150 mM). (b) Transfer curves of papain-functionalized (rGO-SiNH$_2$/rGO-N) FETs in 100 times diluted synthetic urine containing different concentrations of cystatin C.

and biosensors without the need for sophisticated microfabrication steps.

CRediT authorship contribution statement

Fabrício A. dos Santos: Methodology, Data curation, Investigation, Formal analysis, Writing - original draft. **Nirton C.S. Vieira:** Conceptualization, Methodology, Data curation, Writing - original draft, Project administration, Writing - review & editing. **Naiara A. Zambianco:** Methodology, Validation. **Bruno C. Janegitz:** Conceptualization, Supervision, Writing - review & editing. **Valtencir Zucolotto:** Funding acquisition, Conceptualization, Supervision, Resources, Project administration, Writing - review & editing.

Declaration of Competing Interest

The authors declare that they have no known competing financial interests or personal relationships that could have appeared to influence the work reported in this paper.

Acknowledgments

The authors are grateful for the financial support provided by Conselho Nacional de Desenvolvimento Científico e Tecnológico (CNPq: 300878/2016-8, 447001/2014-0 and 303338/2019-9) and São Paulo Research Foundation (FAPESP: 17/21097-3, 17/21898-6 and 18/07508-3). The authors thank the Brazilian Nanotechnology National Laboratory/Brazilian Center for Research in Energy and Materials (LNNano/CNPEM) for the availability of the infrastructure for the microfabrication of the interdigitated electrodes, in particular, the researchers Maria Helena de Oliveira Piazzetta and Angelo Luiz Gobbi (Microfabrication Laboratory) and Juliana da Silva Bernardes and Bruna Pomin Massucato for the XPS measurements.

Appendix A. Supplementary material

Supplementary data to this article can be found online at https://doi.org/10.1016/j.apsusc.2020.148698.

References

[1] K.S. Novoselov, A.K. Geim, S.V Morozov, D. Jiang, Y. Zhang, S.V. Dubonos, I.V. Grigorieva, A.A. Firsov, Electric field effect in atomically thin carbon films, Science (80-.). 306 (2004) 666–669.

[2] N.C.S. Vieira, J. Borme, G. MacHado, F. Cerqueira, P.P. Freitas, V. Zucolotto, N.M. R. Peres, P. Alpuim, Graphene field-effect transistor array with integrated electrolytic gates scaled to 200 mm, J. Phys. Condens. Matter. 28 (2016), https://doi.org/10.1088/0953-8984/28/8/085302.

[3] D.R. Dreyer, S. Park, C.W. Bielawski, R.S. Ruoff, The chemistry of graphene oxide, Chem. Soc. Rev. 39 (2010) 228–240.

[4] S. Pei, H.-M. Cheng, The reduction of graphene oxide, Carbon N. Y. 50 (2012) 3210–3228.

[5] Q. He, S. Wu, S. Gao, X. Cao, Z. Yin, H. Li, P. Chen, H. Zhang, Transparent, flexible, all-reduced graphene oxide thin film transistors, ACS Nano. 5 (2011) 5038–5044.

[6] B. Chitara, L.S. Panchakarla, S.B. Krupanidhi, C.N.R. Rao, Infrared photodetectors based on reduced graphene oxide and graphene nanoribbons, Adv. Mater. 23 (2011) 5419–5424.

[7] M. Zhou, Y. Zhai, S. Dong, Electrochemical sensing and biosensing platform based on chemically reduced graphene oxide, Anal. Chem. 81 (2009) 5603–5613.

[8] F. Yan, M. Zhang, J. Li, Solution-Gated Graphene Transistors for Chemical and Biological Sensors, Adv. Healthc. Mater. 3 (2014) 313–331.

[9] Y.-M. Lei, M.-M. Xiao, Y.-T. Li, L. Xu, H. Zhang, Z.-Y. Zhang, G.-J. Zhang, Detection of heart failure-related biomarker in whole blood with graphene field effect transistor biosensor, Biosens. Bioelectron. 91 (2017) 1–7.

[10] X. Chen, Y. Liu, X. Fang, Z. Li, H. Pu, J. Chang, J. Chen, S. Mao, Ultratrace antibiotic sensing using aptamer/graphene-based field-effect transistors, Biosens. Bioelectron. 126 (2019) 664–671.

[11] W.S. Chang, H. Jeong, J.H. Kim, S. Lee, M. Wajahat, J.T. Han, S.H. Cho, S.K. Seol, Micropatterning of reduced graphene oxide by meniscus-guided printing, Carbon N. Y. 123 (2017) 364–370.

[12] T. Lee, S.H. Min, M. Gu, Y.K. Jung, W. Lee, J.U. Lee, D.G. Seong, B.-S. Kim, Layer-by-layer assembly for graphene-based multilayer nanocomposites: synthesis and applications, Chem. Mater. 27 (2015) 3785–3796.

[13] D.W. Lee, T.-K. Hong, D. Kang, J. Lee, M. Heo, J.Y. Kim, B.-S. Kim, H.S. Shin, Highly controllable transparent and conducting thin films using layer-by-layer assembly of oppositely charged reduced graphene oxides, J. Mater. Chem. 21 (2011) 3438–3442.

[14] H. Hwang, P. Joo, M.S. Kang, G. Ahn, J.T. Han, B.-S. Kim, J.H. Cho, Highly tunable charge transport in layer-by-layer assembled graphene transistors, ACS Nano. 6 (2012) 2432–2440.

[15] H. Li, Q. Yu, B. Yang, Z. Li, L. Lei, Electro-catalytic oxidation of artificial human urine by using BDD and IrO2 electrodes, J. Electroanal. Chem. 738 (2015) 14–19.

[16] B.C. Janegitz, F.A. dos Santos, R.C. Faria, V. Zucolotto, Electrochemical determination of estradiol using a thin film containing reduced graphene oxide and dihexadecylphosphate, Mater. Sci. Eng. C. 37 (2014) 14–19.

[17] S. Umrao, T.K. Gupta, S. Kumar, V.K. Singh, M.K. Sultania, J.H. Jung, I.-K. Oh, A. Srivastava, Microwave-assisted synthesis of boron and nitrogen co-doped reduced graphene oxide for the protection of electromagnetic radiation in Ku-band, ACS Appl. Mater. Interfaces. 7 (2015) 19831–19842.

[18] D.S. Kim, V. Dhand, K.Y. Rhee, S.-J. Park, Study on the effect of silanization and improvement in the tensile behavior of graphene-chitosan-composite, Polymers (Basel). 7 (2015) 527–551.

[19] I.G. Arruda, F.E.G. Guimarães, R.J. Ramos, N.C.S. Vieira, Self-assembly of SiO<inf>2</inf>nanoparticles for the potentiometric detection of neurotransmitter acetylcholine and its inhibitor, J. Nanosci. Nanotechnol. 14 (2014), https://doi.org/10.1166/jnn.2014.9351.

[20] N.C.S. Vieira, A. Figueiredo, J.F. Dos Santos, S.M. Aoki, F.E.G. Guimarães, V. Zucolotto, Label-free electrical recognition of a dengue virus protein using the SEGFET simplified measurement system, Anal. Methods. 6 (2014), https://doi.org/10.1039/c4ay01803f.

[21] N.C.S. Vieira, W. Avansi, A. Figueiredo, V.R. Mastelaro, V. Zucolotto, Potentiometric detection of chemical species by spin-assisted assembly of vanadium pentoxide nanorods, Sens. Actuators B Chem. 229 (2016), https://doi.org/10.1016/j.snb.2016.02.010.

[22] A. Nieto, F. Balas, M. Colilla, M. Manzano, M. Vallet-Regí, Functionalization degree of SBA-15 as key factor to modulate sodium alendronate dosage, Microporous Mesoporous Mater. 116 (2008) 4–13.

[23] B. Konkena, S. Vasudevan, Understanding aqueous dispersibility of graphene oxide and reduced graphene oxide through p K a measurements, J. Phys. Chem. Lett. 3 (2012) 867–872.

[24] Z. Lin, G. Waller, Y. Liu, M. Liu, C. Wong, Facile synthesis of nitrogen-doped graphene via pyrolysis of graphene oxide and urea, and its electrocatalytic activity toward the oxygen-reduction reaction, Adv. Energy Mater. 2 (2012) 884–888.

[25] X. Li, H. Wang, J.T. Robinson, H. Sanchez, G. Diankov, H. Dai, Simultaneous nitrogen doping and reduction of graphene oxide, J. Am. Chem. Soc. 131 (2009) 15939–15944.

[26] Z. Luo, S. Lim, Z. Tian, J. Shang, L. Lai, B. MacDonald, C. Fu, Z. Shen, T. Yu, J. Lin, Pyridinic N doped graphene: synthesis, electronic structure, and electrocatalytic property, J. Mater. Chem. 21 (2011) 8038–8044.

[27] A. Ganguly, S. Sharma, P. Papakonstantinou, J. Hamilton, Probing the thermal deoxygenation of graphene oxide using high-resolution in situ X-ray-based spectroscopies, J. Phys. Chem. C. 115 (2011) 17009–17019.

[28] A.L.M. Reddy, A. Srivastava, S.R. Gowda, H. Gullapalli, M. Dubey, P.M. Ajayan, Synthesis of nitrogen-doped graphene films for lithium battery application, ACS Nano. 4 (2010) 6337–6342.

[29] X. Fan, W. Peng, Y. Li, X. Li, S. Wang, G. Zhang, F. Zhang, Deoxygenation of exfoliated graphite oxide under alkaline conditions: a green route to graphene preparation, Adv. Mater. 20 (2008) 4490–4493.

[30] X. Wang, W. Xing, P. Zhang, L. Song, H. Yang, Y. Hu, Covalent functionalization of graphene with organosilane and its use as a reinforcement in epoxy composites, Compos. Sci. Technol. 72 (2012) 737–743.

[31] R. Scaffaro, L. Botta, G. Lo Re, R. Bertani, R. Milani, A. Sassi, Surface modification of poly (ethylene-co-acrylic acid) with amino-functionalized silica nanoparticles, J. Mater. Chem. 21 (2011) 3849–3857.

[32] E. Piccinini, C. Bliem, C. Reiner-Rozman, F. Battaglini, O. Azzaroni, W. Knoll, Enzyme-polyelectrolyte multilayer assemblies on reduced graphene oxide field-effect transistors for biosensing applications, Biosens. Bioelectron. 92 (2017) 661–667.

[33] E. Stern, R. Wagner, F.J. Sigworth, R. Breaker, T.M. Fahmy, M.A. Reed, Importance of the Debye screening length on nanowire field effect transistor sensors, Nano Lett. 7 (2007) 3405–3409.

[34] J. Brzin, T. Popovič, V. Turk, U. Borchart, W. Machleidt, Human cystatin, a new protein inhibitor of cysteine proteinases, Biochem. Biophys. Res. Commun. 118 (1984) 103–109.

[35] D. Desai, A. Kumar, D. Bose, M. Datta, Ultrasensitive sensor for detection of early stage chronic kidney disease in human, Biosens. Bioelectron. 105 (2018) 90–94.

[36] H. Lin, L. Li, C. Lei, X. Xu, Z. Nie, M. Guo, Y. Huang, S. Yao, Immune-independent and label-free fluorescent assay for Cystatin C detection based on protein-stabilized Au nanoclusters, Biosens. Bioelectron. 41 (2013) 256–261.

[37] X. Gu, J. Gao, X. Li, Y. Wang, Immobilization of Papain onto graphene oxide nanosheets, J. Nanosci. Nanotechnol. 18 (2018) 3543–3547.

[38] D.-J. Kim, I.Y. Sohn, J.-H. Jung, O.J. Yoon, N.-E. Lee, J.-S. Park, Reduced graphene oxide field-effect transistor for label-free femtomolar protein detection, Biosens. Bioelectron. 41 (2013) 621–626.